EXPLORING THE MORPHOLOGY OF HIGH-RESOLUTION 3D PRINTED SCAFFOLDS FOR TISSUE ENGINEERING

by

ANDREW AHN

A THESIS

Presented to the Department of Biochemistry
and the Robert D. Clark Honors College
in partial fulfillment of the requirements for the degree of
Bachelor of Science

May 2022

An Abstract of the Thesis of

Andrew Ahn for the degree of Bachelor Science
in the Department of Biochemistry to be taken June 2022

Title: Exploring the Morphology of High-Resolution 3D Printed Scaffolds for Tissue Engineering

Approved: *Paul Dalton, PhD*
Primary Thesis Advisor

Three-dimensional (3D) printing or additive manufacturing (AM) is a technique that is commonly used within tissue engineering and regenerative medicine (TERM). Among AM techniques, melt electrowriting (MEW) is known for its high-resolution capabilities, which utilizes thermoplastic matersials to produce scaffolds with microscale structures for tissue engineering (TE). Although more popular in recent years, MEW is still underdeveloped, causing the majority of MEW scaffolds utilized within TE to have a 0°/90° laydown pattern. This study explores different laydown pattern (0°/90°, 0°/60°/120°, and 0°/36°/72°/108°/144°) scaffolds made of poly(ε-caprolactone) (PCL) and how these scaffolds are morphologically different and affect cell seeding. The results show that cell seeding was similar between all of the different laydown patterns, with a more even distribution found in the 0°/36°/72°/108°/144°) scaffold due to the better 3D interconnectivity found in this design.

Acknowledgements

I would like to thank Professor Paul Dalton for his supervision and support and providing this great opportunity to explore the world of tissue engineering and additive manufacturing in this past year. His continuous support and environment that he has created in the Dalton lab has allowed me to meet build many friendships, learn, and grow. I would also like to thank Professor Marian Hettiaratchi and Professor Trond Jacobsen for joining my Thesis Committee and their support. I would like to also thank the people at the Clark Honors College at the University of Oregon in working through the relevant procedures.

A special thanks goes to Dr. Biranche Tandon, who was a kind, wonderful mentor, and a great friend. I would also like to thank Taavet Kangur and Simon Luposchainsky who helped in understanding g-code programming and 3D printing. Additional thanks to Dr. Angela Lin who helped with microCT imaging and understanding it, as well as Kelly O'Neill who was essential in SEM imaging and for her support. I would also like to thank Dr. Ievgenii Liashenko for assisting with the generation of g-code for MEW scaffolds. Broadly, I would like to thank everyone in the Dalton lab and the people at the Phil and Penny Knight Campus who provided advice, support, and all the time we spent together. Finally, I would like to thank my family for their unconditional support throughout this process.

Table of Contents

List of Figures

List of Tables

Chapter 1: Introduction

1.1 Overview

Additive manufacturing (AM) – commonly referred to as 3D printing – is an increasingly used technology in university-based research and in industry due to its high customizability and ability to quickly alter complex computer generated designs for production (Shahrubudin *et al*., 2019). One research area where AM is embraced is in tissue engineering and regenerative medicine (TERM) as researchers attempt to better replicate the complex structures of natural tissue. Despite decades of research using traditional manufacturing processes, there remains a disconnect between the capabilities of nature to form tissues and humankinds' attempt to fabricate functional tissue to address injuries and disease (Almouemen *et al*., 2019). Among the many AM technologies, melt electrowriting (MEW) is an emerging 3D printing technique that allows for the fabrication of highly ordered and precise structures on the micrometer scale. However, this technology is still developing and despite the increased use of MEW, there is still much to be explored at a basic level (Robinson *et al*., 2019). For MEW to become more widely adopted, protocols and basic know-how of how MEW scaffolds function in the presence of cells/tissues requires further investigation.

1.2 Problem Statement

By having decades of research and development, many established AM technologies have increased in complexity and improved their user interfaces and available software tools. Research groups such as Dr. Paul Dalton's lab have demonstrated the fabrication of complex MEW scaffolds (Liashenko *et al*., 2020),

however the most commonly used MEW scaffolds are substantially simpler (Han *et al*., 2020). With a 0°/90° grid-like laydown pattern being uncomplicated to program, this is the geometry that is primarily used for MEW scaffolds in TE. This is linked to the requirement to directly generate g-code for MEW rather than use software tools that are widely adopted for other, more developed AM technologies. However, this 0°/90° laydown pattern greatly reduces the number of cells that would attach to the scaffold, due to the small diameter fibers that MEW produces. The mechanical properties of 0°/90° laydown pattern scaffolds are also highly dependent on the direction of external forces which is especially important for *in vivo* experiments. However, the multiple layers of fibers that are stacked on one another within this grid-like structure creates fiber walls which limits the cells interaction with other cells on the scaffold. This last point results in MEW uniaxial scaffold porosity in the z-direction, rather than a three-dimensional (3D) porosity in all cartesian axes - a common requirement within TERM. As a consequence of this, there are limitations on how MEW scaffolds can be utilized within TERM. This thesis investigates more complex laydown patterns and their resulting changes in scaffold morphology as well as the effects this may have on tissue engineering applications.

1.3 Objective

The primary objective of this thesis is to observe how shifting away from 0°/90° laydown patterns affect the scaffold morphology, porosity, and cell seeding efficiency.

Chapter 2: Literature Review

2.1 Tissue Engineering and Regenerative Medicine (TERM)

TERM aims to produce biological mimicking tissues for diagnostic and research purposes to cure injuries or diseases (Berthiaume *et al*., 2011). To achieve this, a scaffold or matrix combined with living cells or biologically active tissue is used (Melchels *et al*., 2012). Generally speaking, tissue engineering (TE) is closely related to regenerative medicine, however, there are slight differences where the latter implies the use of cells as a source, while TE uses various biocompatible biomaterials to create tissue-like structures (Berthiaume *et al*., 2011).

To successfully manufacture a TE construct, besides cells, a scaffold or matrix is required; two words that are often interchangeably used but technically different. A scaffold commonly refers to a solid support structure for cells with an interconnected open pore network (Melchels *et al*., 2012). A matrix, however, is typically a hydrogel, which is a cross-linked polymeric network that is able to swell and contain large amounts of water, but does not dissolve (Ahmed, 2015; Melchels *et al*., 2012). Both scaffolds and matrices are expected to support cell growth, migration, differentiation, and colonization (Melchels *et al*., 2012). However, these constructs also require various mechanical and biological properties designed to closely match the extracellular matrix (ECM) of the target tissue trying to be created. Some properties that are taken into consideration during scaffold or matrix creation are things such as stiffness, strength, surface chemistry, degradation, kinetics, cytotoxicity, *etc*. The biological properties of a scaffold largely depend on the material that is used, so oftentimes this is first selected for its biological compatibility (Gao *et al*., 2016). Mechanical properties, on the other

hand, are altered through the use of materials or the micro-architecture of the scaffold or matrix (Malda *et al*., 2005). Due to limitations with both biomaterials and manufacturing techniques, however, it has proven difficult to identify the necessary properties for scaffolds/matrices to ideally mimic the ECM.

2.2 3D Printing

AM has been increasingly used within the TERM world, providing new avenues for patient-specific scaffolds and implants to be manufactured, which has been increasingly studied around the globe (Khalyfa *et al*., 2007). This evolved from rapid prototyping, where AM was used to produce customized parts that could later be manufactured at volume with other techniques (Paxton *et al*., 2021). The AM process allows researchers to quickly fabricate complex 3D structures and create a physical object from a digital geometrical representation, via the successive addition of materials in layers (Ambrosi & Pumera, 2016; Shahrubudin *et al*., 2019).

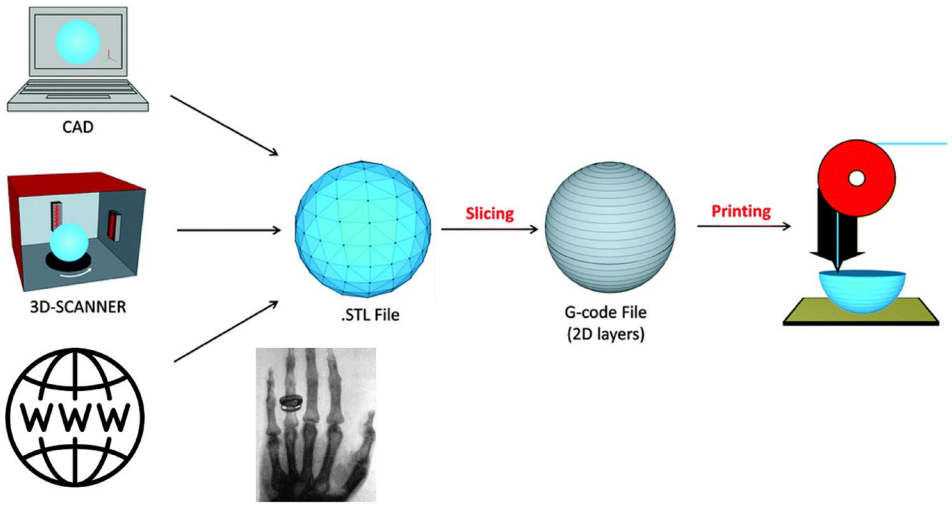

Figure 1. The AM process chain

An overview of the workflow for AM or 3D printing: an .STL file is obtained or generated, sliced into 2D layers to create a g-code file which the machine will interpret to fabricate a 3D object. Adapted from (Ambrosi & Pumera, 2016).

The AM process most commonly starts with obtaining a Standard Tessellation Language (.STL) file that can be generated from several sources, as shown in Figure 1. Some of these sources include computer aided design (CAD), medical imaging, laser scanning, or from a repository on the internet. The .STL file itself is a surface map of an object that consists of a series of triangles that can be readily manipulated in its digital form (Szilvśi-Nagy & Mátyási, 2003). Next in the AM process is slicing, where the .STL file is "sliced" into several layers of a set thickness. After the slicing step, the g–code is generated, creating a set of instructions required by the 3D printer to fabricate the object (Ambrosi & Pumera, 2016).

Within TERM, AM is often used to create scaffolds or matrices, due to its capabilities of fabricating structures that have mathematically predictable physical properties which are tunable and reproducible allowing for detailed studies on various aspects of TERM (Melchels *et al*., 2012). There are a number of 3D printing

technologies that are used within the TERM world for the fabrication of scaffolds, ranging from fused deposition modeling (FDM), stereolithography (SLA), 3D bioprinting, digital light processing and many more (Melchels *et al*., 2012; Petcu *et al*., 2018). Such AM techniques have their advantages and disadvantages, including whether the technology is capable of processing suitable materials for biomedical applications. With established AM technologies only able to produce a limited range of implants, there is a focus on emerging technologies that can provide a suitable cell environment and have a mechanically sufficient structure with high-resolution, all while being reproducible (Melchels *et al*., 2012).

Additionally, AM has already seen clinical use, resulting in personalized implants for use within humans. Examples include medical models, saw guides, dental implants, and even a cell-free cranial implant, as can be seen below in figure 2.

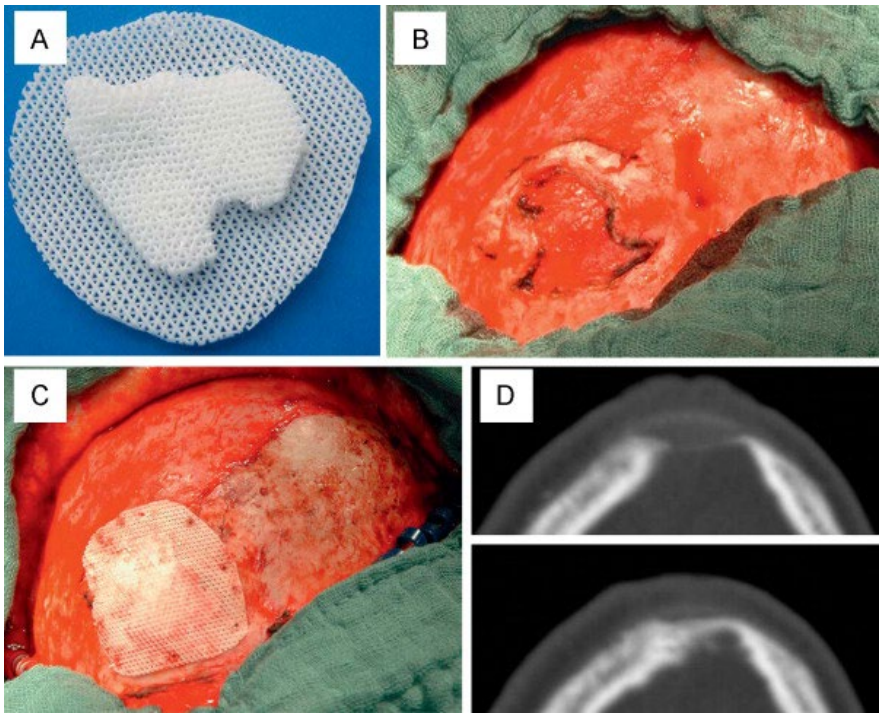

Figure 2. Example of clinical cell-free AM implant

Calvarial reconstruction using polycaprolactone-calcium phosphate scaffolds designed from CT imaging data and fabricated by FDM. Scaffold implant designed by medical CT scan and fabricated by FDM (A). Calvarial defect (B). Defect after scaffold implanted (C). CT scan showing beginning of bone regeneration in defect after 6 months (D)(Probst *et al*., 2010).

2.3 Melt Electrowriting (MEW)

MEW is a solvent-free AM technique that is increasingly used within TERM for its high-resolution printing capabilities on the micrometer scale (Saidy *et al*., 2020; Youssef *et al*., 2019). Using a high voltage and a configuration as shown in figure 3, MEW is capable of consistently fabricating fibers between 2-50 μm (Youssef *et al*., 2019) with the smallest MEW fibers in literature to date being 820 nm (Hochleitner *et al*., 2015). These fibers are then used to create highly ordered and reproducible structures. To better understand how thin these fibers can be, figure 4 shows a comparison of a planar and complex tubular MEW scaffold, a hair, and FDM extrusion.

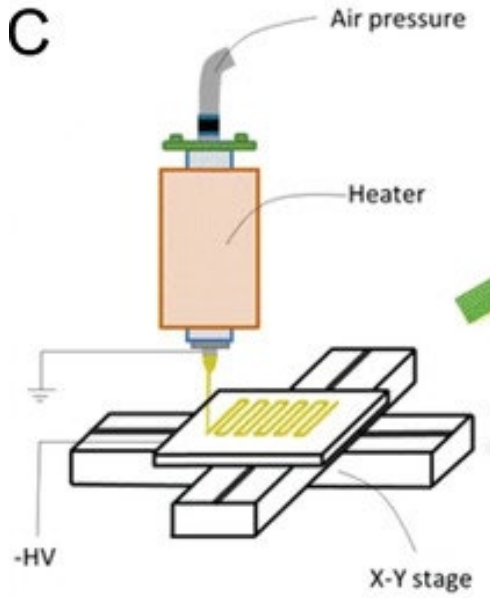

Figure 3. Schematic of MEW process

Inside the print head is a heater that maintains a polymer melt with an applied air pressure. High voltage is applied between a collector attached to a motorized x-y stage and the print head in order to create a thin and continuous fiber from the polymer melt (Zeng *et al*., 2018).

Figure 3 shows how the thinning of the molten jet in MEW results in a substantially smaller diameter fiber than the nozzle from which it originates. The applied voltage allows this thin jet to be sustained at low flow rates, in the range of 5 µL/H (Böhm *et al*., 2022). MEW processes a polymer melt while other AM techniques that operate on similar scales often require volatile solvents that are cytotoxic, so the need for these extra expenses are removed.

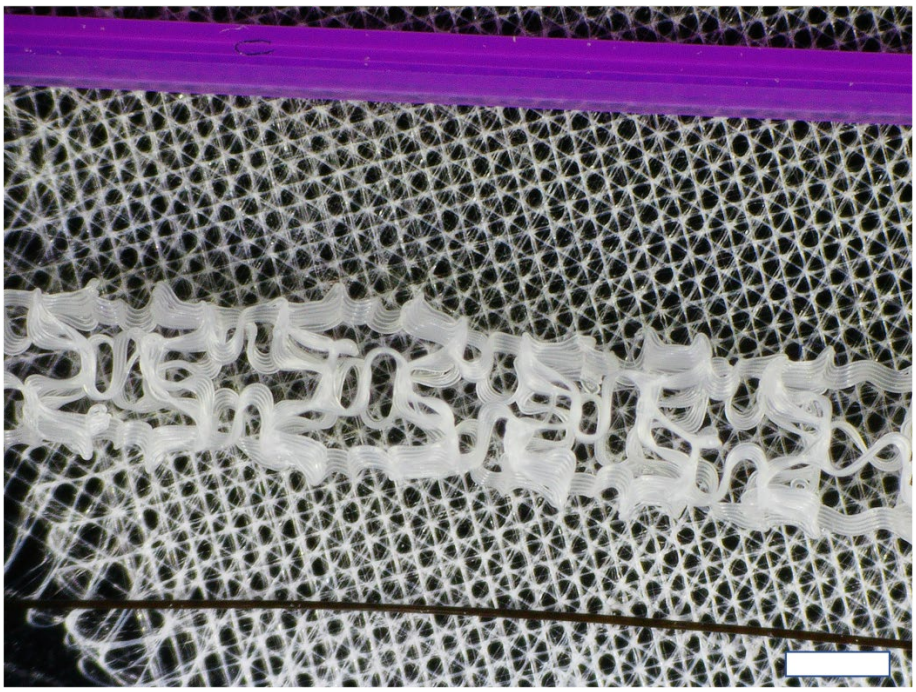

Figure 4. Photograph providing a context of scale

This figure displays 5 layers of FDM extrusion (purple), a complex tubular MEW scaffold (white), a hair (black), and a planar MEW scaffold (white) to give more context to the scale at which MEW operates. Scale bar is 1mm.

Being similar to melt-extrusion printing, MEW provides similar benefits but with high resolution structures, which is an increasingly popular area of research within the biomedical world. Specifically, MEW scaffolds have been investigated within several areas, including use as TERM scaffolds (Han *et al*., 2020), for cancer research (Jørgensen *et al*., 2020), as *in vitro* tools and models (Dufour *et al*., 2022), and as implantable biomaterials *in vivo* (Abbasi *et al*., 2020). However, the majority of cell studies are completed using basic 0°/90° laydown pattern scaffolds (Han *et al*., 2021) exemplified in figure 5.

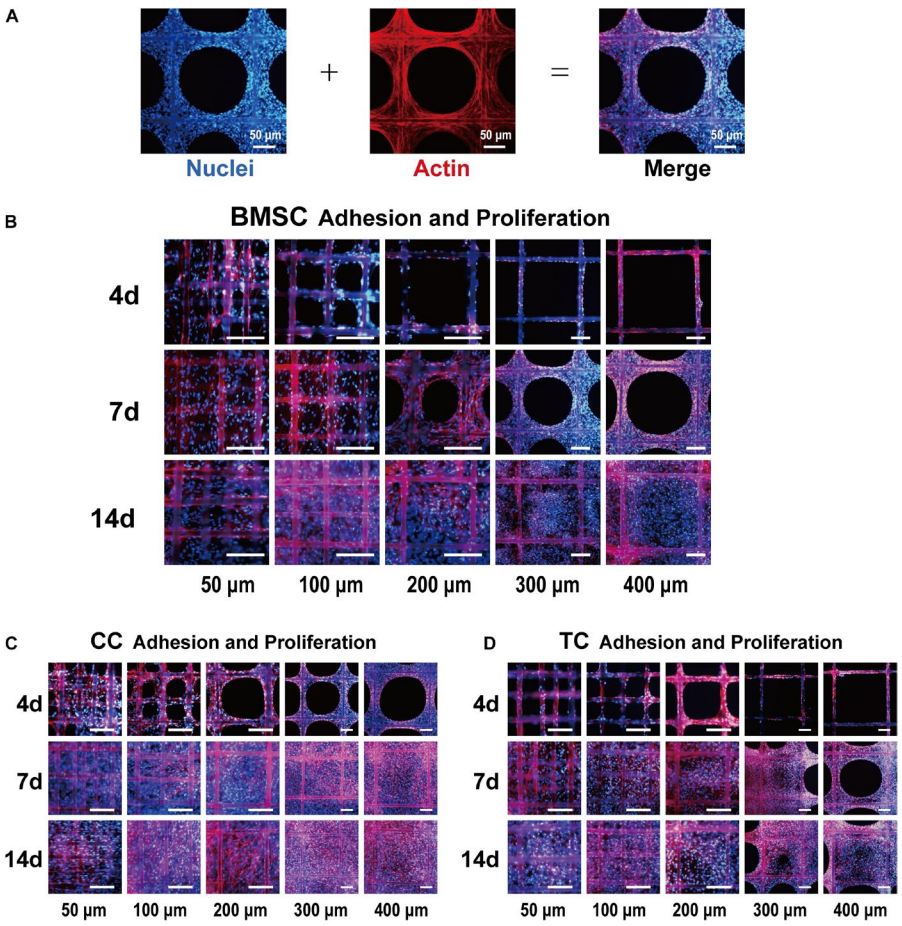

Figure 5. Fluorescence images of MEW scaffolds and bone marrow MSCs

Representative image of cell-loaded scaffolds, the left showing DAPI (blue) stained nuclei, middle shows phalloidin (red) labeled actin and the right shows the merged image (A). Fluorescence images of bone marrow MSCs (B). Chondrocytes (C) Tendon cells on 50, 100, 200, 300, and 400 µm porous MEW scaffolds at 4, 7 and 14 days. Scale bars are 100 µm. (Han *et al*., 2021)

There have been previous studies with MEW scaffolds, that explored areas such as pore size, however, they do not utilize more complex geometries (Han *et al*., 2020). Figure 5 shows how proliferating ECM-producing cells, aggregate at the fiber-fiber intersections and form circular “whorls”, resulting in a hole in the middle of the scaffold pores that eventually becomes filled in. This group has also explored, how these pores as seen in figure 5 affects cell morphology.

However, there is still much more to be uncovered. Mechanical properties are one such area of exploration, where a 0°/90° laydown pattern MEW scaffold has significantly different properties depending on the direction of the force applied. More complex printing, including small microscale shifts in the laydown pattern have been shown to significantly affect the mechanical strength (Liashenko *et al*., 2020). This is important since MEW is used for different tissues and organs that each have their own requirements for scaffold design.

In general, the simple 0°/90° laydown pattern is used because of its programming simplicity and lack of available digital tools for MEW scaffold design. Despite there being some literature that has produced more complex MEW scaffold designs akin to what is seen in this thesis, these geometries are often not utilized for cell studies (Youssef *et al*., 2019). This project focuses on how more complex scaffolds can be designed, made, and characterized with respect to TERM and other biomedical applications.

Chapter 3: Materials and Methods

3.1 MEW Scaffolds

Materials used within this study were used as provided.

3.1.1 Materials

Medical grade poly(ε-caprolactone) (PCL) was purchased from Corbion (PURASORB PCL PC12 lot no. 200701461, September 2021, The Netherlands) and aliquoted into 50 mL Falcon tubes and stored at -80°C until use. The MEW printers used for the fabrication of all scaffolds in this study are custom designs, with an example of the Queensland University of Technology (QUT) MEW printer built in Australia in Appendix A. PCL was prepared by heating in a drying oven at 90°C for 3-4 days in a plastic syringe with a 25-G nozzle, where it was then placed in the print head for use.

A common type of MEW printer system, such as the QUT printer consists of a print head in which two electrical heaters maintain the molten state of the PCL while pressure is applied to the syringe. The print head was mounted on a z-directional stage and a custom-made aluminum collector was moved utilizing z-y linear stages. A potential difference was applied to the nozzle and the collector. A second configuration with reversed polarity is used within the UO printer with slightly different heaters. Printed scaffolds were collected on 25 mm x 75 mm glass slides and stored at room temperature. Scaffolds were laser cut into 6 mm diameter circles using a laser cutter (Universal Laser Systems Inc., USA).

3.1.2 MEW Process Parameters

The scaffolds were printed with a target spacing of 250 μm between two fibers and a fiber diameter of 10 μm. Since the MEW community relies heavily on custom-built systems, two different printers were utilized for this study to ensure reproducibility. Both printers used within this study are of standard builds within the Dalton Lab, the QUT printer MEW head, which is an older build, has been part of many different research publications (Luposchainsky, 2021; Wunner *et al*., 2019). Whereas the UO printer, with slight differences in the MEW head, is a newly built MEW system at the University of Oregon (UO), USA, that was commissioned in December 2021.

The printing parameters for the three different laydown patterns for the scaffolds utilized in this study were kept almost identical. Due to the target spacing, fiber diameter desired, and differences in the build and design of the printers, however, the printing parameters between the QUT and UO printers are different. For the QUT printer, a set temperature of 90°C was used to melt the PCL, with an applied air pressure of 1.5 bar. The molten polymer was pushed out of the nozzle ~3 mm above the collector as the collector moved at a speed of 450 mm/min. A voltage of 4.8 kV was applied between the nozzle and collector. For the UO printer, a set temperature of 75°C was used to melt the PCL, with an applied pressure of 1.25 bar. The molten polymer was pushed out of the nozzle ~3 mm above the collector with an applied voltage of 5.0 kV as the collector moved at a speed of 450 mm/min.

3.1.3 MEW Scaffold Laydown Patterns

The MEW scaffolds were printed with fibers in three different laydown patters, 0°/90°, 0°/60°/120°, and 0°/36°/72°/108°/144°. These three laydown patterns will be

referred to as 90x2x10, 60x3x7, and 36x5x4 scaffolds, respectively. The scaffold nomenclature is based off the scaffold architecture with the first number being the angle at which the next set of fibers are being placed, with the second number describing the number of times that angle offset is happening, and the third number describing the number of stacked fibers at non-intersection points.

3.1.4 Printing Tool Path

Scaffold designs were generated using the computer program MATLAB (MathWorks, USA) with custom code provided by Dr. Ievgenii Liashenko (Figure 6) where the generated code was then transcribed into g-code that is compatible with the printer system. A full example of the MATLAB g-code generator can be found in appendix B.

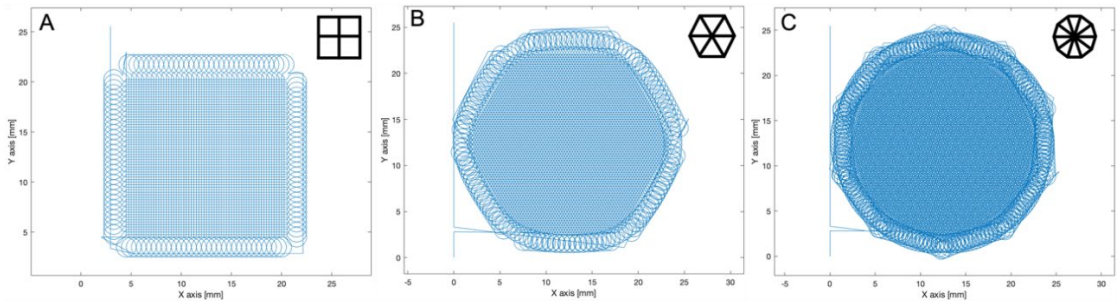

Figure 6. MATLAB g-code generation

MATLAB generated print path for 90x2x10 scaffold (A), 60x3x7 (B), and 36x5x4(C).

3.2 Scaffold Imaging Techniques

3.2.1 Scanning Electron Microscopy (SEM)

An Apreo 2 SEM (ThermoFisher Scientific, USA) was used for SEM imaging to visualize the scaffold structure and morphology. The MEW scaffolds were mounted on stubs with carbon tape and directly imaged without sputter coating. One scaffold of each geometry from both QUT and UO MEW printers were imaged utilizing SEM.

3.2.2 Microcomputed Tomography (microCT)

The microCT scans of the MEW scaffolds were collected using a Zeiss Xradia 620 Versa (Zeiss, Germany) to visualize the design as well as the cross-sectional area of each structure. One scaffold of each type was mounted to a plastic holder (Coin Capsules, Hicarer, China) and scanned using the following parameters: a voltage of 60 kV and a power of 6.5 W with a range of 1.73-3.39 μm pixel resolution. The two-dimensional (2D) images were then reconstructed and processed into a 3D image with the system software package Dragonfly (Object Research Systems, Canada).

3.3 Cell Culture

3.3.1 Cell Seeding

Human mesenchymal stem cells (hMSCs) were obtained from an anonymous donor from the periodontal ligament and were kindly provided by the Willet Lab at the University of Oregon. The cells were stored in liquid nitrogen and were thawed for this experiment.

Laser cut scaffolds were sterilized for cell culture by soaking them in 200 proof ethanol for 1 hour in a Petri dish and subsequently transferred into the center of the wells of a sterile non-tissue culture treated 48-well plate. The well plates with scaffolds were then placed in the incubator at 37°C to dry overnight.

On the following day, in a (1300 SERIES A2) cell culture hood, the scaffolds were then seeded with 1414 cells in 20 μL of growth media of 10% fetal bovine serum (FBS and 1% penicillin-streptomycin (P/S)) as a droplet on top of each laser cut MEW scaffold and incubated at 37°C and 5% CO_2. After 6 hours of incubation, cells were washed with phosphate-buffered saline (PBS) and then fixed with 500 μL of 4% paraformaldehyde (PFA) in PBS for 1 hour. Afterwards, the PFA was removed, and the scaffolds washed were with PBS and stored in PBS at 4°C. This was then repeated, but after 24 hours of incubation.

3.3.2 Cell Staining

In a cell culture hood, after the designated incubation time, the PBS in the well plates was removed and the scaffolds were transferred to a new non-tissue culture treated 48 well plate and then soaked in 500 μL of 0.1% Triton-X in PBS for 15 min. The Triton-X was then removed, and the scaffolds were washed with PBS. Afterwards, 500 μL of DAPI (4',6-diamidino-2-phenylidole, 300 nM) stain was added into each well before the entire well plate was wrapped in aluminum foil as the scaffolds and cells soaked in the DAPI solution for 15 minutes. After, the DAPI stain was removed, the scaffolds were washed with PBS and subsequently stored in PBS.

3.3.3 Confocal Imaging and Analysis

The DAPI stained cells and scaffolds were imaged using a Zeiss LSM 880 (Zeiss, USA) with an Airy Scan detector to produce confocal images. The resulting images were then processed utilizing a custom script within the software package distribution Fiji, based on the open source program ImageJ (Schindelin *et al*., 2012).

3.3.4 Statistical Analysis

Data analysis was performed using GraphPad Prism9 (GraphPad, USA). Data was analyzed by 2-way ANOVA tests with $P > 0.05$ considered significant.

Chapter 4: Results and Discussion

4.1 AM process of MEW

MEW, unlike many established AM technologies, is still relatively young and the relevant software tools have not been developed to the same extent. As a result, the MEW process often starts with the direct creation of g-code which is used to control the MEW printer's movement. In addition to this, there is no standard for programming languages or printers used for MEW as the majority of devices that are used within research labs are custom made. More often than not, biomedical researchers interested in using MEW are not well versed in software development, so the writing of g-code is often done manually or with crude custom generation scripts. An example of manually generated g-code can be viewed in Appendix C. In table 1. are some of the g-code commands which are used to manually generate g-code for MEW printers within this particular study.

G1: Linear Interpolation
G2, G3: Circular clockwise or counterclockwise interpolation
G4: Dwell
G17: XY Plane Selection
G21: Programming in millimeters [mm]
G91: Relative Positioning
FXXX: Sets speed of movement [XXX mm/min]

Table 1. G-code commands

These commands are commonly used to create g-code manually for custom MEW printers.

Manual g-coding, however, can be very tedious and often restricts the user to create simple code – an explanation for why the generation of the 0°/90° laydown pattern is so common for MEW (as well as other emerging AM technologies, including 3D bioprinting (Derakhshanfar *et al*., 2018). This is not ideal for TERM research where complex structures are often desired, so a system that can generate g-code in a quick and user-friendly way is still required for MEW. However, the status quo for the majority of research labs is to resort to manually creating the g-code for the creation of MEW of scaffolds.

In this thesis, a simple g-code generation script for MEW printers was used in this study as mentioned in section 3.1.4. There are several parameters that were input into the MATLAB program to generate the MEW scaffold laydown pattern. Some key parameters are listed below in table 2. The g-code generator is a script written by Dr. Ievgenii Liashenko and the resulting g-codes were used in both QUT and UO printers to ensure that the print quality did not differ between printers.

Parameters
Overall length [mm]
Overall width [mm]
Distance between lines [mm]
Number of Layers
Printing speed [mm/min]

Table 2. Parameters used in g-code generation

Some parameters used to define the MEW scaffold design

The g-code generation script used within this study, is primarily meant to take in geometric parameters to generate g-code in the x-y plane. Additional settings such as voltage, air pressure, and z-axis movement, however, are not part of this program. These processes are input manually using a controllable voltage and air pressure system, while the z-axis offset is calibrated by hand using an object of known size. Other g-code settings like selecting x-y movement, programming in millimeters, and relative positioning, also must be manually added to the g-code output made by the script. Then the entire code is used in the MEW printer where the desired scaffolds can be produced.

4.2 SEM

SEM is an imaging technique used to quantitatively measure the diameter of MEW fibers, due to its high resolution and the optical limits of light microscopy at small fiber diameters. The three laydown pattern MEW scaffolds within this study of 90x2x10, 60x3x7, 36x5x4, made on two different MEW printers were imaged, resulting in what can be seen in figure 7. In table 3 below is the average fiber diameter produced by the two different printers as well as the fiber diameters measured between each type of scaffold. With a target fiber diameter of 10 μm, the QUT and UO printers produced an average fiber diameter of 11.62 ± 1.28 μm and 8.59 ± 0.51 μm (n=6). This is a result of the differences between the two printers and the settings used when creating these scaffolds. It also shows the challenges that exist within MEW research as settings will usually differ between MEW systems. Making it difficult to accurately reproduce results due to there not being an overarching existing AM process or workflow.

Scaffold type	Fiber Diameter (µm)	Scaffold Type	Fiber Diameter (µm)
QUT 90x2x10	11.44 ± 1.09	UO 90x2x10	8.44 ± 0.47
QUT 60x3x7	11.27 ± 1.34	UO 60x3x7	8.58 ± 0.64
QUT 36x5x4	12.62 ± 1.38	UO 36x5x4	8.74 ± 0.43
Average	11.62 ± 1.28	Average	8.59 ± 0.51

Table 3. MEW fiber diameters

The following table displays the average fiber diameters calculated using SEM images and ImageJ of the various scaffolds used within this study. (n=6)

Figure 7 displays representative images of the six different types of scaffolds created within this study. No obvious pulsing (irregular changes in fiber diameter) was observed for the fibers within the scaffold as the fibers were found to be uniform with a homogeneous surface. In figure 7E some fiber breaking can be observed (red arrow), although it is difficult to say precisely what caused this to happen, one difference that the 60x3x7 scaffolds have is that the fiber intersections are 21 fibers tall rather than the 20 found in the other two geometries. Fiber breaking however, is not seen in figure 7B, despite sharing the same geometry as the scaffold in figure 7E, which is likely due to the fiber being thicker in 7B compared to 7E. Since the fiber is thinner as well, it will have less mass and thus be more easily influenced by outside forces, and it can be observed that the broken fiber points up rather than down. Thus, it is highly likely that the swap in polarity used in the UO MEW system caused the fiber breaking seen in figure 7E.

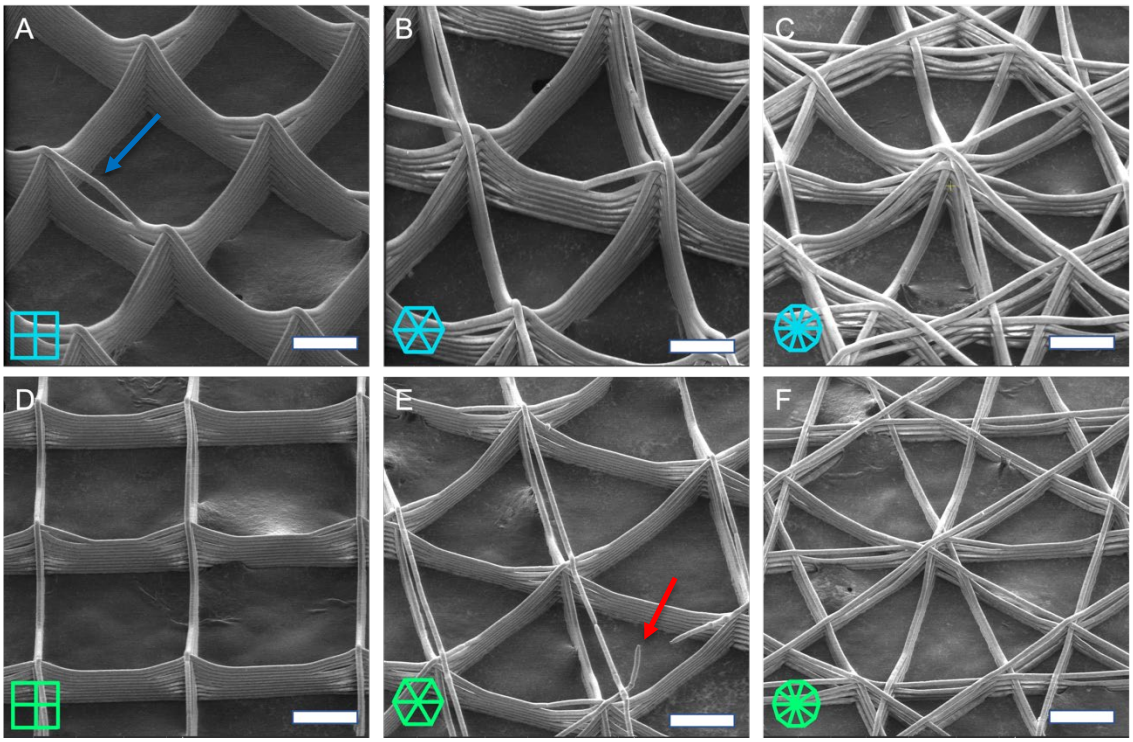

Figure 7. SEM images of the three laydown patterns

SEM images of the three laydown pattern scaffolds produced from two different printers. QUT printed scaffolds (A-C) and UO printed scaffolds (D-F). 90x2x10 scaffold (A, D), 60x3x7 (B, E), and 36x5x4(C, F). Scale bars are 100 μm.

Upon closer inspection of figure 7B, C, E, and F, some fiber suspension can be observed. This effect was reported by (Hrynevich *et al*., 2021) who describes that when interfiber distances in MEW are reduced, fibers can span across air gaps. This fiber suspension consistently appears in the 36x5x4 scaffolds while having the same parallel fiber spacings of 250 μm as the other scaffold designs. Due to the nature of the scaffold design, there is more variation in the number of fibers at any fiber intersection which results in much smaller inter-fiber distances within the scaffold and thus more fiber suspension. However, figures 7B and E still exhibit fiber suspension only on the topmost layers.

A possible explanation for the fiber suspension found in figures 7B and E is because of the charge accumulation, due to the height of the fiber intersections being 21 fibers. It was reported by (Kade & Dalton, 2021) that accumulated charge in the deposited fibers has disrupted MEW scaffold designs before. So, it is likely that the deposited fibers in the 60x3x7 design had accumulated enough charge to repel the final fibers, causing them to be suspended. This can also be seen slightly in figure 7A (blue arrow), but not in figures 7C and F as there are not enough fibers within the stacked portions to accumulate enough charge to repel the next fibers.

The consistent fiber suspension that is seen in the 36x5x4 allows for improved 3D interconnectivity in the x-y plane. Compared to other scaffold geometries such as the 90x2x10 and 60x3x7 laydown patterns that tend to result in less suspended fibers and more “walls” forming. In order to better observe these fiber walls within the scaffolds, a more detailed image of the fiber intersections was taken and can be seen in figure 8 below.

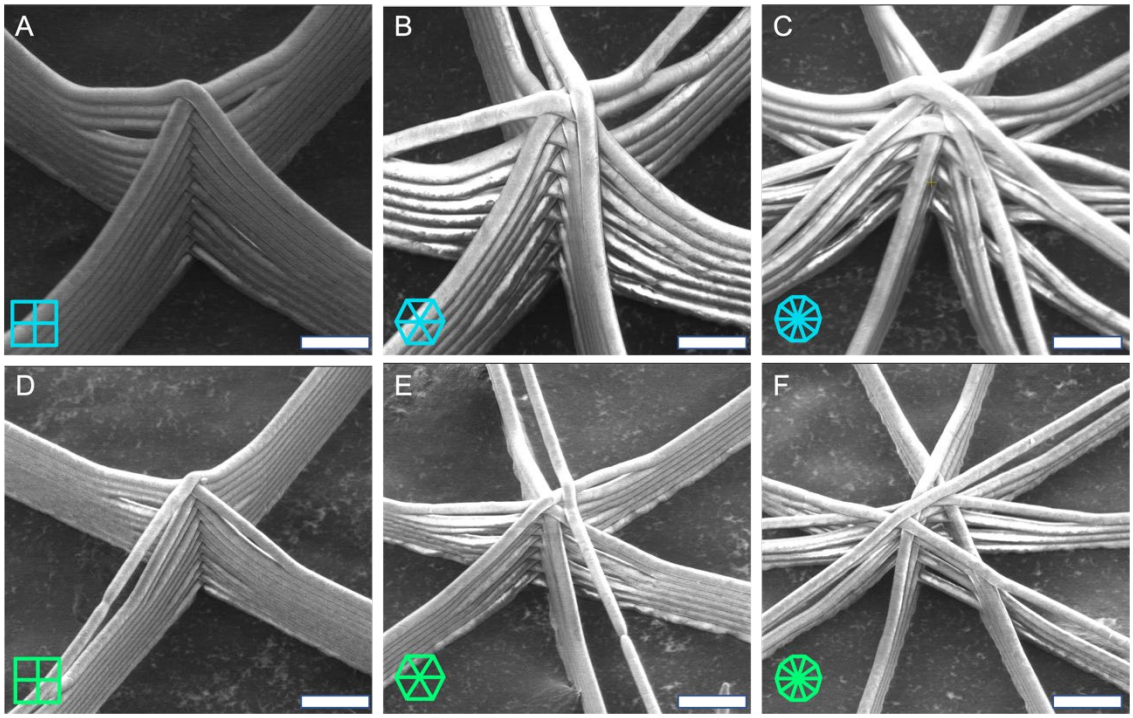

Figure 8. SEM images of fiber intersections

SEM images of the three laydown pattern fiber intersections produced from two different printers. QUT printed scaffolds (A-C) and UO printed scaffolds (D-F). 90x2x10 scaffold (A, D), 60x3x7 (B, E), and 36x5x4(C, F). Scale bars are 50 μm.

With a magnified view of the fiber intersections in figure 8, a total of 20 fibers are stacked at the junctions for the 90x2x10 and 36x5x4 MEW scaffolds while the 60x3x7 scaffolds had a total of 21 stacked fibers. The stacking behavior of fibers for the 90x2x10 and the 60x3x7 scaffolds can be observed to have little to no gap between fibers, forming a fiber wall. However, in the 36x5x4 scaffold the fibers are stacked such that there appears to be gaps between fibers and thus does not have these fiber walls, allowing for better 3D interconnectivity throughout the x-y plane of the scaffold. The relevance behind the 3D interconnectivity found in the 36x5x4 scaffolds appears later when discussing the cell studies and imaging. Although the 3D interconnectivity of the

scaffolds can somewhat be observed utilizing SEM, there are limitations in what SEM is capable of in terms of easily imaging the micro-architectures within the scaffolds.

4.3 MicroCT

MicroCT is a non-destructive imaging technique that uses x-rays to determine the shape and structure of an object. It is often used in medicine for understanding internal organ structures, but for this study microCT imaging is done to small scaffolds to determine the spatial resolution of a scaffold (Youssef *et al*., 2019).

With microCT however, one limitation with using SEM is resolved, as it creates a manipulable 3D representation of the scaffold. This allows for better and quantitative observation of scaffold 3D interconnectivity that is not readily achieved using SEM imaging. MicroCT was performed for each of the scaffolds within this study to provide views and images of scaffolds from different angles and magnifications. A quick 3D overview of the scaffolds with slight differences in brightness of the false coloring can be seen below in figures 9 and 10.

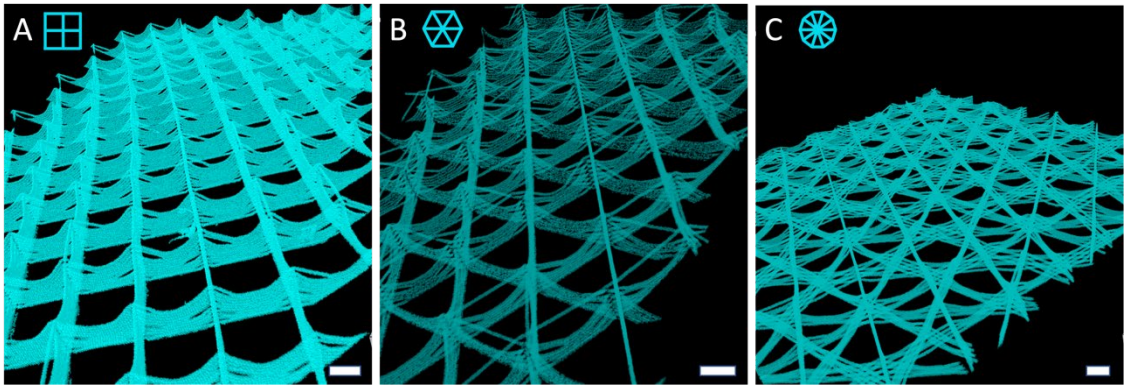

Figure 9. MicroCT scans of QUT printed MEW scaffolds

A 3D overview of the QUT 90x2x10 (A), 60x3x7 (B), and 36x5x4(C) printed MEW scaffolds, with false coloring. Scale bars are 100 μm.

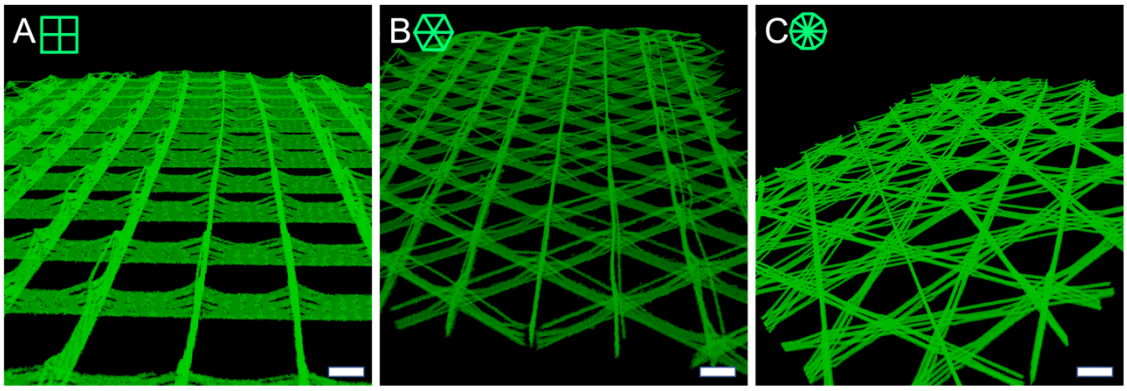

Figure 10. MicroCT scans of UO printed MEW scaffolds

A 3D overview of the UO 90x2x10 (A), 60x3x7 (B), and 36x5x4(C) printed MEW scaffolds, with false coloring. Scale bars are 100 μm.

It can be seen, that in figures 9 and 10, there is a high contrast between the scaffold (false colored while processing the image), as well as the background to observe the 3D interconnectivity. There is also the additional transparency of the scaffold that is observed in the microCT scans which is not the case for the SEM images. The transparency or opaqueness of the scaffold for each microCT image is controlled during image processing by varying the intensity of the false coloring used. This, in turn, allows for a better visualization of fibers that are closest in terms of perspective while also observing the fibers behind those as well, giving a more detailed overview of the scaffolds compared to using just SEM.

Similar to the findings in the SEM images, figures 9 and 10C show that fiber suspension is consistently found throughout the scaffold, which is not as prevalent in figures 9 and 10A and B. Comparing fiber suspension between the microCT and SEM images, this phenomenon is easier to observe with microCT, unlike the SEM due to the line-of-sight nature of SEM photography. In figures 9 and 10A and B, fiber walls are observed and additional details that are not as noticeable in the SEM images such as the

small openings within the fiber walls in figures 9 and 10A and B can be seen. The same phenomenon of the fiber suspension found in figures 7B and E, can also be seen in figures 9 and 10B as well as the fiber breaks in 9B.

MicroCT scans also display 2D slices or cross-sectional areas of the object being scanned, which in this case can be used to further confirm that there is 3D interconnectivity. Figure 11 below, shows a close up on the of the cross-sectional image of the MEW scaffold fiber walls.

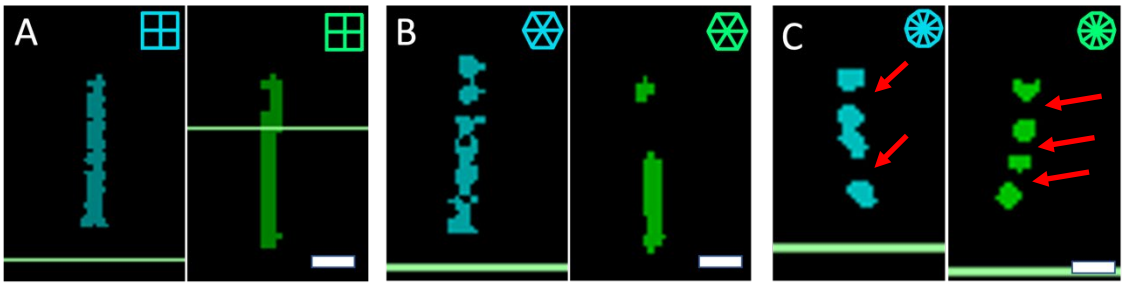

Figure 11. MicroCT scan 2D cross section of QUT and UO MEW scaffolds.

2D slices, focusing on fiber walls of the QUT (cyan) and UO (green) 90x2x10 (A), 60x3x7 (B), and 36x5x4(C) MEW scaffolds. Scale bars are 20 μm. The green line is used to navigate through the 2D slices provided by the microCT scan.

Figure 11 directly compares the fiber walls of the QUT and UO printed MEW scaffolds, and it can be observed in figure 11A and B that these walls are prevalent throughout these scaffolds. Additional details like the suspended fiber found in the 3D overviews in figure 10 can also be found in the UO scaffold in figure 9B. Figure 11C, on the other hand, clearly displays the individual fibers within the 36x5x4 MEW scaffold (red arrows). Compared to the other images, a clear separation of each individual fiber is observed, showing that there is indeed more 3D interconnectivity in

the x-y plane rather than the more one directional interconnectivity found in the 90x2x10 and 60x3x7 MEW scaffolds.

Volume thickness mapping was also performed, as seen below in figure 12, of the resulting microCT scans with a blue green coloring. With the blue color indicating thinner areas, whereas the yellow color signifies thicker areas. Histograms were also produced as a result of the volume thickness mapping, where the frequency at which the volume thickness can be observed as seen in figure 13. This was done to see how the microCT scans calculated the resulting fiber diameters compared to those that were measured with the SEM scans. While also visually observing, if there were large variations in fiber thicknesses utilizing the 3D false coloring which resulted in the blue and yellow colors seen in figure 12.

Within the software program Dragonfly, used to process the microCT scans, the volume thickness mapping measures from a central voxel, which are 3D pixels, used to generate the 3D reconstruction that can be seen in figure 12. From this central voxel the program calculates the number of voxels that are connected to this voxel in a sphere around it until it hits an empty voxel. Then it calculates the thickness of these connected voxels and represents this thickness as changes in colors as seen in figure 12. And because the program doesn't know exactly where to start its measurements, there are some measurements that are done in the center of a fiber as well as some that are closer to the edge of the fibers. This results in some measurements stopping before reaching the other side of the fiber, marking these areas as being 'thinner' because the measurements hit an empty voxel.

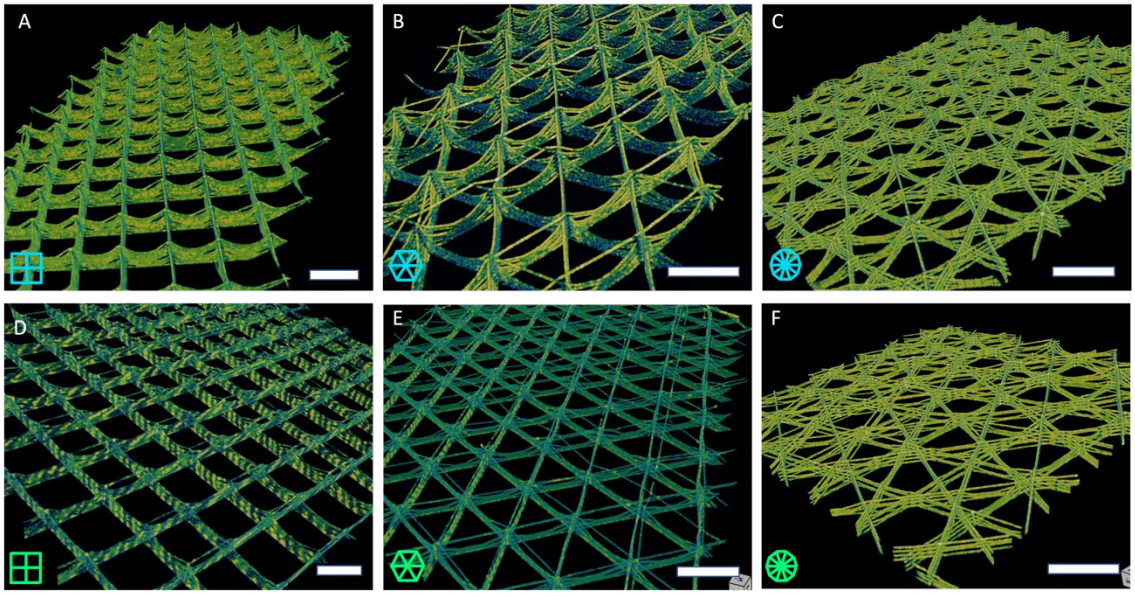

Figure 12. Volume Thickness Mapping using MicroCT of MEW scaffolds

3D images, of volume thickness mapping with the blue and yellow colors indicating thinner and thicker areas respectively. QUT printed scaffolds (A-C) and UO printed scaffolds (D-F). 90x2x10 scaffold (A, D), 60x3x7 (B, E), and 36x5x4(C, F). Scales bars are 250 µm.

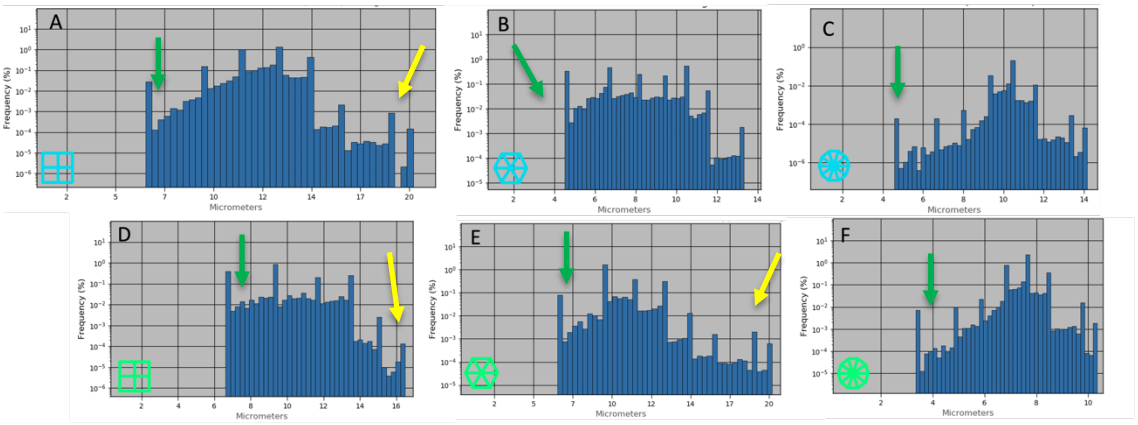

Figure 13. Volume Thickness Histograms generated using MicroCT

The y-axis displays the frequency on a logarithmic scale in which a section of the scaffold at a certain thickness in micrometers (x-axis) appears. QUT printed scaffolds (A-C) and UO printed scaffolds (D-F). 90x2x10 scaffold (A, D), 60x3x7 (B, E), and 36x5x4(C, F).

MicroCT scans can also be used to compare the values found in the volume thickness mapping in the microCT scans with the SEM fiber diameter calculations. In the histograms shown above in figure 13, it is observed that there seems to be a wide range of thicknesses found within each of the microCT scans. Overall, the microCT scans seem to at least follow the trend that was found in table 2 and include the fiber diameters that were calculated. However, due to the way that the volume thickness mapping is calculated, as mentioned previously, the images in figure 13 indicate that there are "thinner" areas (green arrows) within the scaffold, when in reality these scaffolds are uniform in fiber diameter as found in SEM imaging. In areas within figure 13A, D, and E, there are thicker areas (yellow arrows). This is likely due to portions of the laser cut MEW scaffold being imaged, as a laser/heat is used in cutting the scaffolds. This laser melts portions of the scaffold, which leads to the polymer fibers to melt together, thus the melted portion of the scaffold is being calculated as thicker than the other fibers. These specific measurements, however, cannot be used to do any quantitative calculations as there is too much variability not to mention that the volume thickness mapping is not an accurate representation of the fiber diameters. Thus, this processing and the data generated is primarily used to view if the fibers seem to be rather consistent in thickness as well as confirming that the fiber diameters measured in table 2 are precise.

4.4 Cell Culture

The MEW scaffolds were seeded with hMSCs in order to investigate how the cells would attach to an untreated MEW scaffold made with PCL and if there were any differences in the cell count on the scaffolds. MSCs were selected due to prior evidence of these particular cells being used with MEW scaffolds. Some previous examples include the seeding of different types of MSCs onto a 90x2 laydown pattern MEW scaffold (Han *et al*., 2021; Hochleitner *et al*., 2015).

The MEW scaffolds within this study were seeded with a small 20 μL droplet with hMSCs on top of the laser cut scaffold, meaning that there is only a portion of the scaffold that the bubble is in contact with which would be the region of interest when doing any imaging or analysis. Interestingly, there was no significant difference in the cell counts measured between the different geometries. Figure 14 shows the average number of cells found on each of the scaffolds after 6 and 24 hours, within the region of interest. It was found that overall, there seemed to be more cells on MEW scaffolds that were created using the QUT printer, compared to the UO printer scaffolds, which is likely a result of the thicker fibers found in the former.

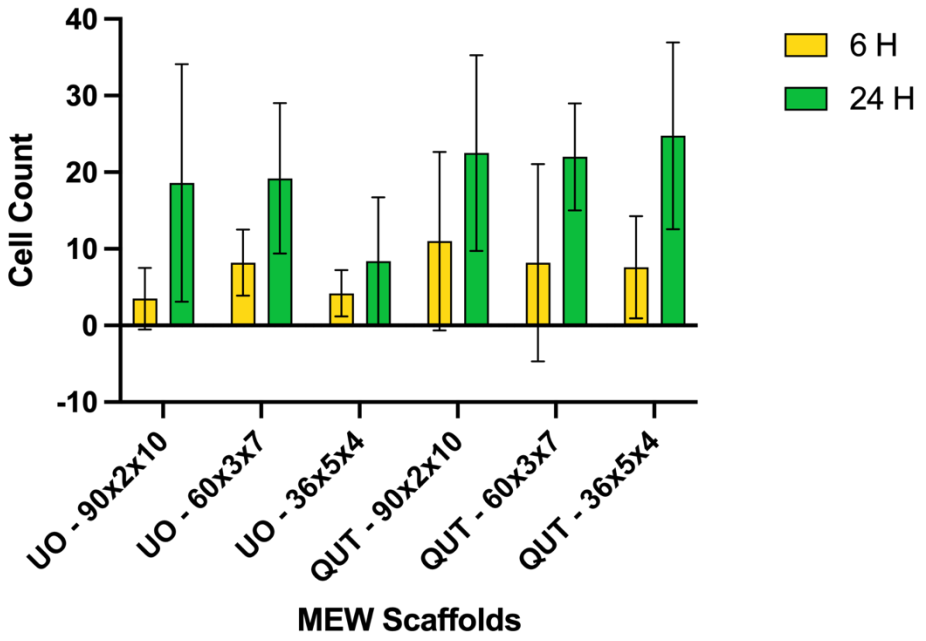

Figure 14. Average cell counts on respective scaffolds at the 6 H and 24 H time points

This graph displays the average cell counts of each type of scaffold used within this study at both 6hr and 24 H time points while also showing the standard deviation found between each of the samples. Across time points $p < 0.0001$. (n=5 for each type of scaffold used)

As seen in figure 14 above, there is a significant amount of standard deviation between each of the cell counts, which is likely a result of excessive handling while staining the cells. This could be interpreted as the data used within this study is unreliable, but there are still a few things that can be observed through this data. First, the error bars throughout each sample are rather large. However, the general pattern found with the overall cell counts between the two time points appears to be consistent between samples. Indicating that the general pattern can still be trusted, and to further reaffirm this, a statistical significance calculation was done, and it was found that these results are significant. However, this error is as mentioned a result of transferring the

cell-laden scaffolds to a different plate which was required for confocal imaging which agitated the cells on the scaffolds causing them to fall off.

The similarity in the average cell counts on the MEW scaffolds can be attributed to the cell-seeding method that was used. By attaching the cells using a droplet method on top of the scaffold, it ensures that the cells are suspended on top of the scaffold, giving time for them to attach to the nearest structure which would be the MEW scaffold rather than the well plate. When utilizing this method and directly imaging after a short period of time, however, has the draw back in that our region of interest is only within a portion of the scaffold and the image taken does not cover the entire area. Since the droplet of cells does not cover as much of the scaffold, the area imaged might not be representative or the intended area where the data was collected, which is why we see a significantly lower number of cells compared to the original seeded number. Although, this can be seen as a large issue, because this is done for all of the samples, it ensures that there is no bias in simply imaging the area with the most cells. Allowing for a more accurate representation of the data found in this study.

Confocal microscopy is a method that is commonly used to image cells in 3D, and in this study, the nuclei of the MSCs were stained with DAPI. Some 2D slices of the confocal images of the 6 different MEW scaffolds at the 6 and 24 hour time points are displayed below in Figure 15 and 6 respectively.

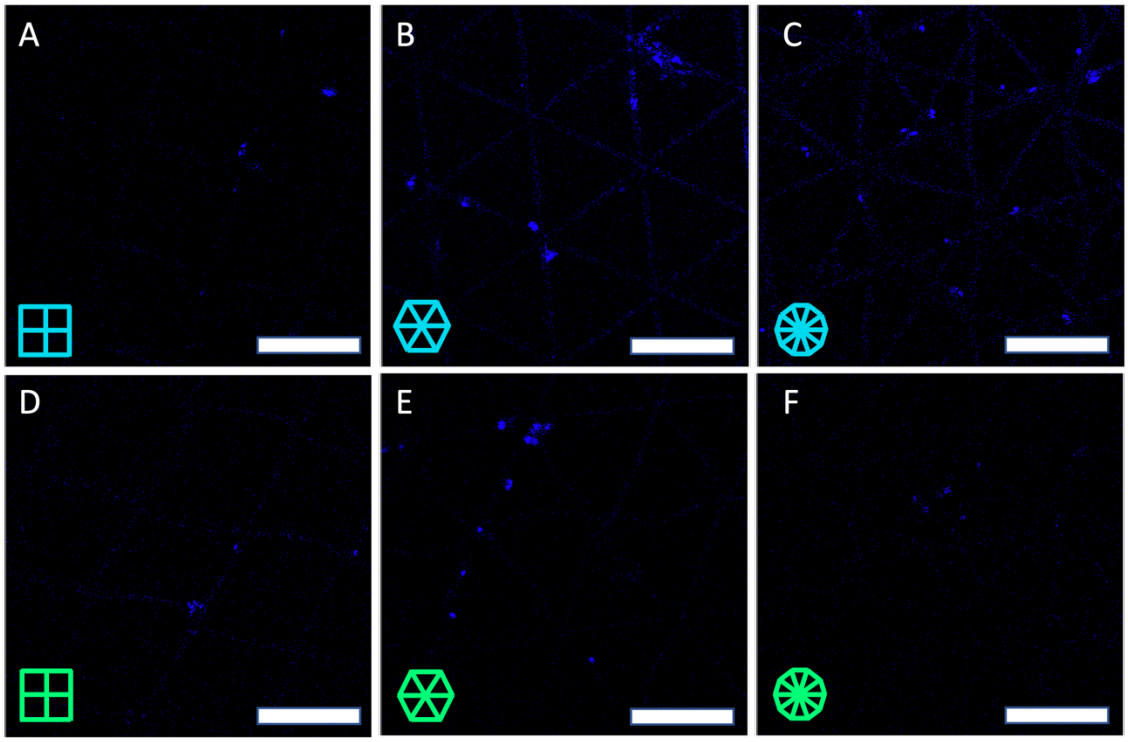

Figure 15. Confocal of 6-hour time point

This figure displays confocal images of cell nuclei stained with DAPI as bright blue spots, with MEW scaffold being slightly visible. QUT printed scaffolds (A-C) UO printed scaffolds (D-F). 90x2x10 scaffold (A, D), 60x3x7 (B, E), and 36x5x4(C, F). Scale bar is 250 μm.

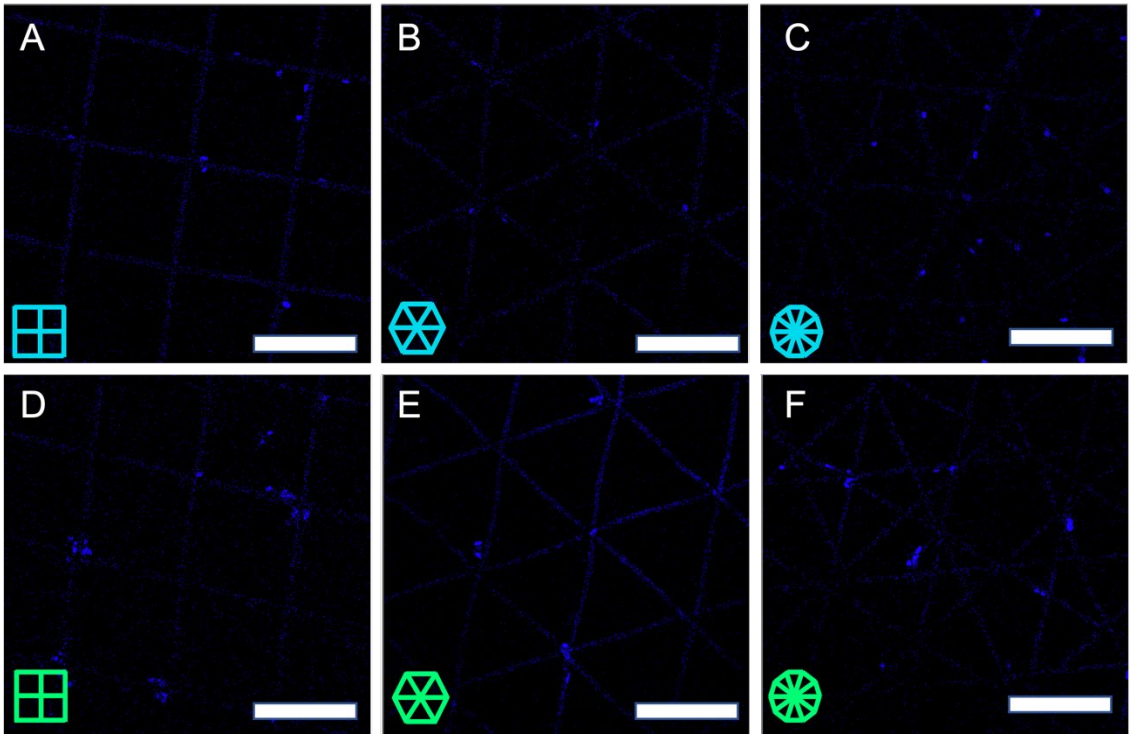

Figure 16. Confocal images of 24-hr time point

This figure displays of the confocal images of cell nuclei stained with DAPI as bright blue spots, with MEW scaffold being slightly visible. QUT printed scaffolds (A-C) UO printed scaffolds (D-F). 90x2x10 scaffold (A, D), 60x3x7 (B, E), and 36x5x4(C, F). Scale bar is 250 μm.

On closer inspection, in all of the images in figures 15 and 16, there is some background noise as well as the MEW scaffold being visible. This is a result of the hydrophobic nature that PCL, the material used in the creation of the scaffolds, and DAPI, the stain used in these images, have. Due to both materials being hydrophobic the DAPI stain gets adsorbed onto the surface of the scaffold allowing for the observation of where the cells attach to the scaffold. If both the DAPI and PCL were opposite in nature, it would have resulted in some random background noise and primarily cells showing up in the confocal image without knowing where these cells are on the scaffold, which could be problematic. The noise caused by the MEW scaffolds,

does not cause any issues when doing cell counts using ImageJ, as they are filtered out resulting in the brightest spots which are the nuclei of the MSCs to show up, providing an accurate cell count.

Despite the previous mentions of the possible unreliability of the quantitative data, one thing that is qualitatively observed in figures 15 and 16, is that the congregation of cells appears to show some sort of pattern. Generally, it can be observed that the cells are bunched around the fiber intersections, where there is less distance to bridge between the individual fibers on the scaffold structure. This can clearly be seen in figure 15B and E as well as figure 16D, and F as cells can be seen gathering in the corners. This has also been observed in previous studies utilizing MSCs where cells tended to congregate around the corners of the scaffold morphology (Han *et al*., 2021). However, these fiber intersection points are much more numerous in the 36x5x4 MEW scaffolds and observing figures 15C and F and figures 16C and F, it appears that the cells are more spread out and evenly spaced from each other rather than clumped in specific areas.

The clumps of cells that can be seen in figures 15 and 16 are not ideal for TE in that it would cause issues with evenly distributing nutrients to other cells, hindering cell growth. It is difficult to say what the exact cause of the cell clumping in the 90x2x10 and 60x3x7 scaffolds is and whether this is from the cells being poorly suspended in the seeding media, clumping post-seeding, or having grown to a significant degree after 24 hours. However, the cells are not given much time to grow as they were only in 20 μL of cell growth media and although they have a certain level of growth between the 6H and 24H time points seen in figure 15, it is unlikely that a single cell was able to grow

to such an extent. It is also, unlikely that this is due to poorly suspended cell media as a more even distribution of cells can be found on the 36x5x4 scaffolds. One reason as to why it is observed that the cells exhibit this behavior could be due to the 36x5x4 scaffolds having better 3D interconnectivity as discussed before. Resulting in less fiber walls in which cells are cornered between within the scaffold as previously mentioned in figure 8.

Chapter 5. Conclusions

In this work, high-resolution scaffold structures were explored with regard to morphology, porosity, and changes in cell seeding efficiency. To achieve this, scaffolds were designed and programmed into two different MEW printers – a commercial and a locally built one. It was found that the scaffolds were similar between the two different printers, although some differences in printing conditions were required. To produce the scaffolds for morphological assessment and cell culture, three different types of geometries were produced from both printers, with 90x2 representing the scaffold geometry commonly found in MEW literature. More complex MEW scaffolds with different laydown paths of 60x3 and 36x5 were used to observe differences that occur. The scaffold morphology was first explored with SEM where the fibers and fiber-fiber intersections could be observed, where the fibers were found to be homogenous and form fiber walls in all geometries besides the 36x5x4 scaffold. Using microCT, the porosity was explored, and it was found that the 36x5x4 scaffolds have higher porosity and 3D interconnectivity throughout the scaffold. Cell seeding efficiency between the three types of scaffolds was found to have similar average cell counts, but the 36x5x4 scaffold had a more even distribution of cells compared to the other two geometries due to its increased porosity. This work examines scaffolds with complex fiber intersections and 3D porosity or interconnectivity that has utility for biomedical applications.

Chapter 6. Future Directions

As a young AM technology, MEW still has many areas of potential further exploration. These include the standardization of MEW printer hardware as well as creating programming tools that are capable of generating g-code for complex structures for novel applications in TE. Similarly, being able to calibrate two different types of MEW printers in a simple manner would remove the need for significant trial and error adjustments to the printing parameters. Although a script was utilized to generate g-code for this study, there were additional still steps required for the entire MEW process, and to become more streamlined like other common AM techniques, significant work must be done in this area.

Further exploration of complex structures can also be done including biomimetic, sinusoidal, layer shifting (Liashenko *et al*., 2020), tubular scaffolds and much more. The mechanical properties of the scaffolds utilized within this study could also be analyzed, to simulate how the scaffold would be affected if translated into a clinical setting.

Most importantly, investigating and improving the cell seeding processes for in vitro research requires more development. Even though best practices for cell seeding were used, the variation between samples even within the same group were substantial. Even before further research on how cells proliferate and grow on MEW scaffolds, performing an extensive comparison on different seeding techniques and establishing more reproducible outcomes should be performed. Utilizing advanced approaches such as 3D bioprinting or cell aggregate seeding may provide such a route to improve the reproducibility for the seeding MEW scaffolds.

Appendix

Appendix A

Appendix A. QUT MEW printer

Appendix B

```
clc
clear
output = 'AA_Square_10x2layers_v02';
fileID = fopen(output,'w');

F=400;
%layers=1; % doesn't do anything
L=2;    %L=sinus Length
A=0.0;  %A=Amplitude peak-to-peak
OL=16;  %OL=Overal Length in X
W=16;   %W=overal Width in Y
D=0.25; %D=Distance between lines
X0=-OL/2;Y0=-W/2;   %(X0,Y0)starting coordinates
```

Sinus lines and loops

```
t=0; %line number from bottom to top in Y
P(1,:)=[X0-2.5,Y0];
while t<W/D % total number of lines along Y axis

for i=0                         :OL:   OL           %rectangular area
%for i=0+abs(t-0.5*W/D)*0.6*D   :0.2:   OL-abs(t-
0.5*W/D)*0.6*D
%sampling step for G-code generation
    P(end+1,:)=[X0+i,Y0+D*(t)+A/2*sin(i*2*3.14/L)]; %left to right
sinusoids

%    P(end+1,:)=[P(end)+0.1,P(end)+0.1]; %left to right sinusoids
end

P(end+1,:)=[P(end,1)+0.08,P(end,2)-0.38];   %right loop
P(end+1,:)=[P(end,1)+0.22,P(end,2)-0.32];
P(end+1,:)=[P(end,1)+0.32,P(end,2)-0.22];
P(end+1,:)=[P(end,1)+0.38,P(end,2)-0.08];
P(end+1,:)=[P(end,1)+0.38,P(end,2)+0.08];
P(end+1,:)=[P(end,1)+0.32,P(end,2)+0.22];
P(end+1,:)=[P(end,1)+0.22,P(end,2)+0.32];
P(end+1,:)=[P(end,1)+0.08,P(end,2)+0.38];
```

```
 P(end+1,:)=[P(end,1)-0.08,P(end,2)+0.38];
 P(end+1,:)=[P(end,1)-0.22,P(end,2)+0.32];
 P(end+1,:)=[P(end,1)-0.32,P(end,2)+0.22];
 P(end+1,:)=[P(end,1)-0.38,P(end,2)+0.08];
 P(end+1,:)=[P(end,1)-0.38,P(end,2)-0.08];
 P(end+1,:)=[P(end,1)-0.32,P(end,2)-0.22];
 P(end+1,:)=[P(end,1)-0.18,P(end,2)-0.32];


 for i=0:OL:OL           %rectangular area
 %for i=0+abs(t-0.5*W/D)*0.6*D   :0.2:   OL-abs(t-0.5*W/D)*0.6*D
     x=OL-i;
     P(end+1,:)=[X0+x,Y0+D*(t+1)+A/2*sin(2*x*3.14/L)]; %right to left
sinusoids
 end


 P(end+1,:)=[P(end,1)-0.08-D,P(end,2)-0.38];   %left loop
 P(end+1,:)=[P(end,1)-0.22,P(end,2)-0.32];
 P(end+1,:)=[P(end,1)-0.32,P(end,2)-0.22];
 P(end+1,:)=[P(end,1)-0.38,P(end,2)-0.08];
 P(end+1,:)=[P(end,1)-0.38,P(end,2)+0.08];
 P(end+1,:)=[P(end,1)-0.32,P(end,2)+0.22];
 P(end+1,:)=[P(end,1)-0.22,P(end,2)+0.32];
 P(end+1,:)=[P(end,1)-0.08,P(end,2)+0.38];
 P(end+1,:)=[P(end,1)+0.08,P(end,2)+0.38];
 P(end+1,:)=[P(end,1)+0.22,P(end,2)+0.32];
 P(end+1,:)=[P(end,1)+0.32,P(end,2)+0.22];
 P(end+1,:)=[P(end,1)+0.38,P(end,2)+0.08];
 P(end+1,:)=[P(end,1)+0.38,P(end,2)-0.08];
 P(end+1,:)=[P(end,1)+0.32,P(end,2)-0.22];
 P(end+1,:)=[P(end,1)+0.18,P(end,2)-0.32];


 t=t+2;
 end

 %P(end+1,:)=[P(end,1),P(end,2)+1.5];   %connection to next layer
```

```
 %%%%%  ROTATING COORDINATES   %%%%%
 theta=-90; %TO ROTATE CLOCKWISE BY X DEGREES
 R=[cosd(theta) -sind(theta); sind(theta) cosd(theta)]; %CREATE THE
MATRIX
```

```
 P1=P*R'; %MULTIPLY VECTORS BY THE ROT MATRIX
 % theta=-120; %TO ROTATE CLOCKWISE BY X DEGREES
 % R=[cosd(theta) -sind(theta); sind(theta) cosd(theta)]; %CREATE THE
MATRIX
 % P2=P*R'; %MULTIPLY VECTORS BY THE ROT MATRIX

 P=[P;P1];        % appending layers with different angles

 P(end+1,:)=[P(end,1)+1.5,P(end,2)];   %connection to next layer
 P(end+1,:)=[P(end,1),P(end,2)-18];   %connection to next layer
 P(end+1,:)=[P(end,1)-17,P(end,2)];   %connection to next layer

 P=[P;P;P;P;P;P;P;P;P;P];       % 10 periods with 2 different angles (20
layers)




 P=[P+12.5];                                                    % shifting
whole scaffold away from zero coordinate

 %E(1,:)=[0,0];                                                  % first
"Entering" point before printing scaffolds
 %E(2,:)=[0,4.5];                                                % second
point before printing scaffolds
 %P=[E;P];

 P(end+1,:)=[P(end,1)-2.2,P(end,2)+0.5];                           % move
away from printed scaffold
 P(end+1,:)=[P(end,1),P(end,2)+25-2.8];                          % move to
new scaffold

 Yshift=25.3;
 P=[P;                                                          % adding
more scaffolds with shift in Y
 %   P(:,1),P(:,2)+Yshift*1;                                    %line 2
 %     P(:,1),P(:,2)+Yshift*2;                                    %line 3
 %     P(:,1),P(:,2)+Yshift*3;                                    %line 4
 %     P(:,1),P(:,2)+Yshift*4;                                    %line 5
 %     P(:,1),P(:,2)+Yshift*5;                                    %line 6
 %     P(:,1),P(:,2)+Yshift*6                                     %line 7
     ];
```

```
 % theta=0; %TO ROTATE CLOCKWISE BY X DEGREES
 % R=[cosd(theta) -sind(theta); sind(theta) cosd(theta)]; %CREATE THE
MATRIX
 % P=P*R'; %MULTIPLY VECTORS BY THE ROT MATRIX


 %P(end+1,:)=[P(end,1),P(end,2)-25];   %connection to next layer
 %P(end+1,:)=[P(end,1)-20,P(end,2)];   %connection to next layer

 %P(end+1,:)=[X0+3,Y0]; % last point same as forst point


 %P(end+1,:)=[P(end,1)-6,P(end,2)-10.5];
 % P(end+1,:)=[P(end,1)-14,P(end,2)];

 %P=[P;P(:,1)+25,P(:,2);P(:,1),P(:,2)-25;P(:,1)+25,P(:,2)-25];


 %%%%%%%%%%%%%% distance for P %%%%%
 Dis(1,:)=P(1,:);
 for i=2:size(P,1)
 Dis(end+1,:)=[P(i,1)-P(i-1,1),P(i,2)-P(i-1,2)];
 i=i+1;
 end



  plot(P(:,1),P(:,2));   %plotting


 %%%%%%%%%%%%% red lines
 t=0;
 while t<OL/L
     if t==0
     N(1,:)=[X0,Y0];
     else
     %N(end+1,:)=[X0+t*L,Y0];
     end
     %N(end+1,:)=[N(end,1),N(end,2)+W+D];
 t=t+1;
 end
 N(end+1,:)=[X0,Y0];

 %%%%%%%%%%%%%% distance for N %%%%%
 DDis(1,:)=[N(1,1)-P(end,1),N(1,2)-P(end,2)];
```

```
for i=2:size(N,1)
DDis(end+1,:)=[N(i,1)-N(i-1,1),N(i,2)-N(i-1,2)];
i=i+1;
end

hold on
%plot(N(:,1),N(:,2));
xlabel('X axis [mm]')
ylabel('Y axis [mm]')
axis equal
axis padded
hold off
```

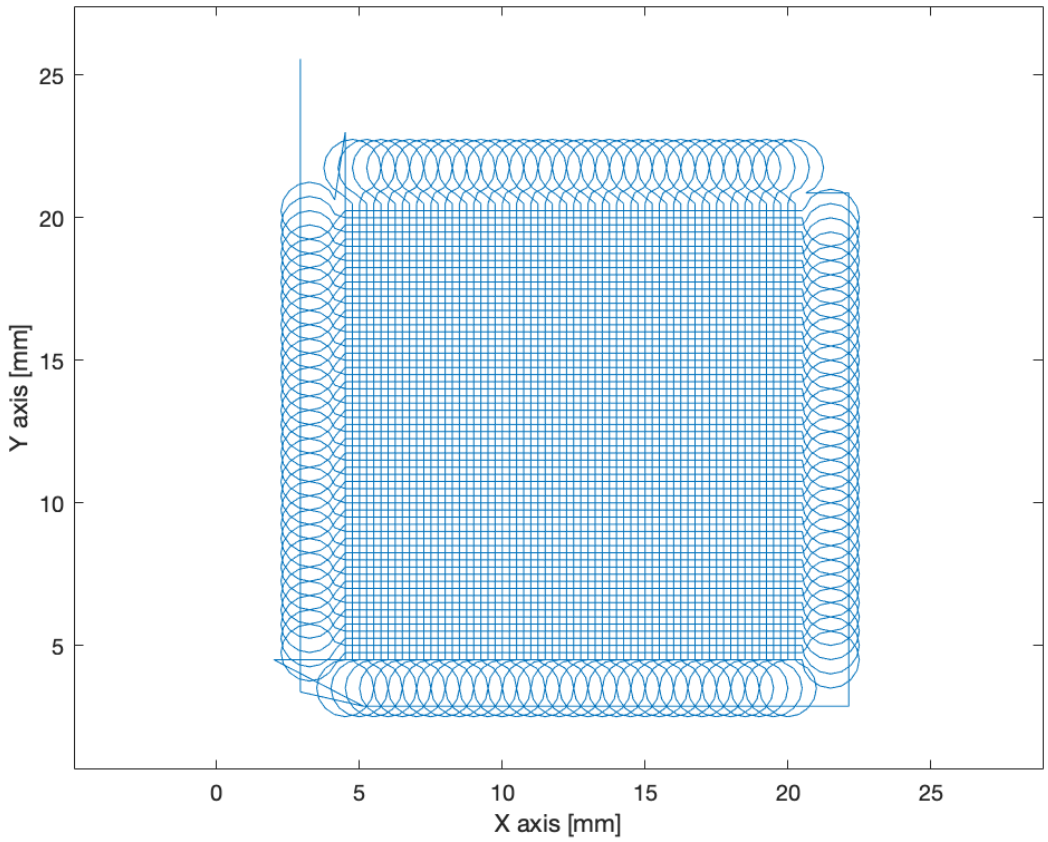


```
%%%%%%% print the Gcode

   i=1;
   C=Dis;
    while i<=size(C,1)
```

```
     gt=['G1 X' num2str(C(i,1),'%.5f') ' Y'
num2str(C(i,2),'%.5f')];           % ' F' num2str(F(3),'%.3f')]; - speed
statement
     fprintf(fileID,'%s' ,gt);    fprintf(fileID,'\r\n');

     i=i+1;
     end
 %
 %
 %        i=1;
 %        C=DDis;
 %     while i<=size(N,1)
 %
 %     gt=['G1 X' num2str(C(i,1),'%.3f') ' Y' num2str(C(i,2),'%.3f') ' F'
num2str(F(3),'%.3f')];
 %     fprintf(fileID,'%s' ,gt);    fprintf(fileID,'\r\n');
 %
 %     i=i+1;
 %     end
```

Appendix B. MatLab g-code generator

Appendix C.

```
%------main-----
G17 G21 G91 (initialization)

F400 (set speed in mm per minute)

g1 x10

M98 p300 l4 (main program loop)

g1 x-10
 (move to starting position)

M30 (end of program)

%------loops-----
o101
g1 x25
g1 x1
g3 x0y0.5 i0.25j0.25
g1 x-1
g1 x-25
g1 x-1
g2 x0y0.5 i-0.25j0.25
g1 x1
M99

o102
g1 y-25
g1 y-1
g2 x-0.5y0 i-0.25j-0.25
g1 y1
g1 y25
g1 y1
g3 x-0.5y0 i-0.25j0.25
g1 y-1
M99

o300
m98 p101 l25
g1 x25
g2 x0y0 i0.5j0.5

m98 p102 l25
g1 y-25
g3 x0y-0 i-0.5j-0.5
M99


%------finish-----
```

Appendix C. Manually written g-code

Bibliography

Abbasi, N., Lee, R. S. B., Ivanovski, S., Love, R. M., & Hamlet, S. (2020). In vivo bone regeneration assessment of offset and gradient melt electrowritten (MEW) PCL scaffolds. *Biomaterials Research*, *24*(1), 17. https://doi.org/10.1186/s40824-020-00196-1

Ahmed, E. M. (2015). Hydrogel: Preparation, characterization, and applications: A review. *Journal of Advanced Research*, *6*(2), 105–121. https://doi.org/10.1016/j.jare.2013.07.006

Almouemen, N., Kelly, H. M., & O'Leary, C. (2019). Tissue Engineering: Understanding the Role of Biomaterials and Biophysical Forces on Cell Functionality Through Computational and Structural Biotechnology Analytical Methods. *Computational and Structural Biotechnology Journal*, *17*, 591–598. https://doi.org/10.1016/j.csbj.2019.04.008

Ambrosi, A., & Pumera, M. (2016). 3D-printing technologies for electrochemical applications. *Chemical Society Reviews*, *45*(10), 2740–2755. https://doi.org/10.1039/C5CS00714C

Berthiaume, F., Maguire, T. J., & Yarmush, M. L. (2011). Tissue Engineering and Regenerative Medicine: History, Progress, and Challenges. *Annual Review of Chemical and Biomolecular Engineering*, *2*(1), 403–430. https://doi.org/10.1146/annurev-chembioeng-061010-114257

Böhm, C., Stahlhut, P., Weichhold, J., Hrynevich, A., Teßmar, J., & Dalton, P. D. (2022). The Multiweek Thermal Stability of Medical-Grade Poly(ε-caprolactone) During Melt Electrowriting. *Small*, *18*(3), 2104193. https://doi.org/10.1002/smll.202104193

Derakhshanfar, S., Mbeleck, R., Xu, K., Zhang, X., Zhong, W., & Xing, M. (2018). 3D bioprinting for biomedical devices and tissue engineering: A review of recent trends and advances. *Bioactive Materials*, *3*(2), 144–156. https://doi.org/10.1016/j.bioactmat.2017.11.008

Dufour, A., Gallostra, X. B., O'Keeffe, C., Eichholz, K., Von Euw, S., Garcia, O., & Kelly, D. J. (2022). Integrating melt electrowriting and inkjet bioprinting for engineering structurally organized articular cartilage. *Biomaterials*, *283*, 121405. https://doi.org/10.1016/j.biomaterials.2022.121405

Gao, Q., Zhu, X., Xiang, J., Lü, Y., & Li, J. (2016). [Strategies to choose scaffold materials for tissue engineering]. *Sheng Wu Gong Cheng Xue Bao = Chinese Journal of Biotechnology*, *32*(2), 172–184. https://doi.org/10.13345/j.cjb.150230

Han, Y., Lian, M., Sun, B., Jia, B., Wu, Q., Qiao, Z., & Dai, K. (2020). Preparation of high precision multilayer scaffolds based on Melt Electro-Writing to repair cartilage injury. *Theranostics*, *10*(22), 10214–10230. https://doi.org/10.7150/thno.47909

Han, Y., Lian, M., Wu, Q., Qiao, Z., Sun, B., & Dai, K. (2021). Effect of Pore Size on Cell Behavior Using Melt Electrowritten Scaffolds. *Frontiers in Bioengineering and Biotechnology*, *9*. https://doi.org/10.3389/fbioe.2021.629270

Hochleitner, G., Jüngst, T., Brown, T. D., Hahn, K., Moseke, C., Jakob, F., Dalton, P. D., & Groll, J. (2015). Additive manufacturing of scaffolds with sub-micron filaments via melt electrospinning writing. *Biofabrication*, *7*(3), 035002. https://doi.org/10.1088/1758-5090/7/3/035002

Hrynevich, A., Achenbach, P., Jungst, T., Brook, G. A., & Dalton, P. D. (2021). Design of Suspended Melt Electrowritten Fiber Arrays for Schwann Cell Migration and Neurite Outgrowth. *Macromolecular Bioscience*, *21*(7), 2000439. https://doi.org/10.1002/mabi.202000439

Jørgensen, M. L., Müller, C., Sikkersoq, M., Nadzieja, M., Zhang, Z., Su, Y., Just, J., Garm Spindler, K.-L., & Chen, M. (2020). A melt-electrowritten filter for capture and culture of circulating colon cancer cells. *Materials Today. Bio*, *6*, 100052. https://doi.org/10.1016/j.mtbio.2020.100052

Kade, J. C., & Dalton, P. D. (2021). Polymers for Melt Electrowriting. *Advanced Healthcare Materials*, *10*(1), 2001232. https://doi.org/10.1002/adhm.202001232

Khalyfa, A., Vogt, S., Weisser, J., Grimm, G., Rechtenbach, A., Meyer, W., & Schnabelrauch, M. (2007). Development of a new calcium phosphate powder-binder system for the 3D printing of patient specific implants. *Journal of Materials Science: Materials in Medicine*, *18*(5), 909–916. https://doi.org/10.1007/s10856-006-0073-2

Liashenko, I., Hrynevich, A., & Dalton, P. D. (2020). Designing Outside the Box: Unlocking the Geometric Freedom of Melt Electrowriting using Microscale Layer Shifting. *Advanced Materials*, *32*(28), 2001874. https://doi.org/10.1002/adma.202001874

Luposchainsky, S. (2021). *Development of a Robotic Platform for Filament-Based Melt Electrowritng of Non-Planar Scaffolds*. University of Würzburg and Queensland University of Technology.

Malda, J., Woodfield, T. B. F., van der Vloodt, F., Wilson, C., Martens, D. E., Tramper, J., van Blitterswijk, C. A., & Riesle, J. (2005). The effect of PEGT/PBT scaffold architecture on the composition of tissue engineered cartilage. *Biomaterials*, *26*(1), 63–72. https://doi.org/10.1016/j.biomaterials.2004.02.046

Melchels, F. P. W., Domingos, M. A. N., Klein, T. J., Malda, J., Bartolo, P. J., & Hutmacher, D. W. (2012). Additive manufacturing of tissues and organs. *Progress in Polymer Science*, *37*(8), 1079–1104. https://doi.org/10.1016/j.progpolymsci.2011.11.007

Paxton, N. C., Dinoro, J., Ren, J., Ross, M. T., Daley, R., Zhou, R., Bazaka, K., Thompson, R. G., Yue, Z., Beirne, S., Harkin, D. G., Allenby, M. C., Wong, C. S., Wallace, G. G., & Woodruff, M. A. (2021). Additive manufacturing enables personalised porous high-density polyethylene surgical implant manufacturing with improved tissue and vascular ingrowth. *Applied Materials Today*, *22*, 100965. https://doi.org/10.1016/j.apmt.2021.100965

Petcu, E. B., Midha, R., McColl, E., Popa-Wagner, A., Chirila, T. V., & Dalton, P. D. (2018). 3D printing strategies for peripheral nerve regeneration. *Biofabrication*, *10*(3), 032001. https://doi.org/10.1088/1758-5090/aaaf50

Probst, F. A., Hutmacher, D. W., Müller, D. F., Machens, H.-G., & Schantz, J.-T. (2010). [Calvarial reconstruction by customized bioactive implant]. *Handchirurgie, Mikrochirurgie, Plastische Chirurgie: Organ Der Deutschsprachigen Arbeitsgemeinschaft Fur Handchirurgie: Organ Der Deutschsprachigen Arbeitsgemeinschaft Fur Mikrochirurgie Der Peripheren Nerven Und Gefasse: Organ Der V...*, *42*(6), 369–373. https://doi.org/10.1055/s-0030-1248310

Robinson, T. M., Hutmacher, D. W., & Dalton, P. D. (2019). The Next Frontier in Melt Electrospinning: Taming the Jet. *Advanced Functional Materials*, *29*(44), 1904664. https://doi.org/10.1002/adfm.201904664

Saidy, N. T., Shabab, T., Bas, O., Rojas-González, D. M., Menne, M., Henry, T., Hutmacher, D. W., Mela, P., & De-Juan-Pardo, E. M. (2020). Melt Electrowriting of Complex 3D Anatomically Relevant Scaffolds. *Frontiers in Bioengineering and Biotechnology*, *8*. https://doi.org/10.3389/fbioe.2020.00793

Schindelin, J., Arganda-Carreras, I., Frise, E., Kaynig, V., Longair, M., Pietzsch, T., Preibisch, S., Rueden, C., Saalfeld, S., Schmid, B., Tinevez, J.-Y., White, D. J., Hartenstein, V., Eliceiri, K., Tomancak, P., & Cardona, A. (2012). Fiji: An open-source platform for biological-image analysis. *Nature Methods*, *9*(7), 676–682. https://doi.org/10.1038/nmeth.2019

Shahrubudin, N., Lee, T. C., & Ramlan, R. (2019). An Overview on 3D Printing Technology: Technological, Materials, and Applications. *Procedia Manufacturing*, *35*, 1286–1296. https://doi.org/10.1016/j.promfg.2019.06.089

Szilvśi-Nagy, M., & Mátyási, Gy. (2003). Analysis of STL files. *Mathematical and Computer Modelling*, *38*(7), 945–960. https://doi.org/10.1016/S0895-7177(03)90079-3

Wunner, F. M., Eggert, S., Maartens, J., Bas, O., Dalton, P. D., De-Juan-Pardo, E. M., & Hutmacher, D. W. (2019). Design and Development of a Three-Dimensional Printing High-Throughput Melt Electrowriting Technology Platform. *3D Printing and Additive Manufacturing*, *6*(2), 82–90. https://doi.org/10.1089/3dp.2017.0149

Youssef, A., Hrynevich, A., Fladeland, L., Balles, A., Groll, J., Dalton, P. D., & Zabler, S. (2019). The Impact of Melt Electrowritten Scaffold Design on Porosity Determined by X-Ray Microtomography. *Tissue Engineering. Part C, Methods*, *25*(6), 367–378. https://doi.org/10.1089/ten.tec.2018.0373

Zeng, J., Wang, H., Lin, Y., Zhang, J., Liang, F., Fang, F., Yang, F., Wang, P., Zhu, Z., Chen, X., Chen, X., Wang, Z., Cai, N., Tang, Y., & Wu, P. (2018). Fabrication of microfluidic channels based on melt-electrospinning direct writing. *Microfluidics and Nanofluidics*, *22*(2), 23. https://doi.org/10.1007/s10404-018-2043-7